Metabolic Engineering Communications 1 (2014) 12–18

Contents lists available at ScienceDirect

Metabolic Engineering Communications

journal homepage: www.elsevier.com/locate/mec

Model-driven identification of dosing regimens that maximize the antimicrobial activity of nitric oxide

Jonathan L. Robinson [a], Richard V. Miller [b], Mark P. Brynildsen [a,b,*]

[a] Department of Chemical and Biological Engineering, Princeton University, Princeton, NJ, USA
[b] Department of Molecular Biology, Princeton University, Princeton, NJ, USA

ARTICLE INFO

Article history:
Received 28 June 2014
Received in revised form
21 August 2014
Accepted 22 August 2014
Available online 1 September 2014

Keywords:
Nitric oxide
Antimicrobial
Escherichia coli
Respiration
Nitric oxide dioxygenase
Hmp
Kinetic model

ABSTRACT

The antimicrobial properties of nitric oxide ($NO^{\bullet}$) have motivated the design of $NO^{\bullet}$-releasing materials for the treatment and prevention of infection. The biological activity of $NO^{\bullet}$ is dependent on its delivery rate, suggesting that variable antimicrobial effects can result from identical $NO^{\bullet}$ payloads dosed at different rates. Using a kinetic model of the *Escherichia coli* $NO^{\bullet}$ biochemical network, we investigated the relationship between $NO^{\bullet}$ delivery rate, payload, and cytotoxicity, as indicated by the duration of respiratory inhibition. At low $NO^{\bullet}$ payloads, the model predicted greater toxicity with rapid delivery, while slower delivery was more effective at higher payloads. These predictions were confirmed experimentally, and exhibited quantitative agreement with measured O_2 and $NO^{\bullet}$ concentrations, and durations of respiratory inhibition. These results provide important information on key design parameters in the formulation of $NO^{\bullet}$-based therapeutics, and highlight the utility of a model-based approach for the analysis of dosing regimens.

1. Introduction

$NO^{\bullet}$ is a highly reactive metabolite whose antimicrobial activity has been harnessed by the immune system to neutralize pathogens (Bogdan, 2001; Fang, 2004; Bowman et al., 2011; Robinson et al., 2014). In recent years, numerous materials that enable controlled release of $NO^{\bullet}$ to infection sites, such as nanoparticles (A. Friedman et al., 2011; A.J. Friedman et al., 2011), patches (Sulemankhil et al., 2012), dendrimers (Sun et al., 2012), and topical creams (Ormerod et al., 2011), have been synthesized, characterized, and shown to exhibit efficacy in treating antibiotic-resistant infections (Schairer et al., 2012; Jones et al., 2010). Two important design parameters of such materials include the rate at which $NO^{\bullet}$ is delivered, and the total payload that can be administered. We recently discovered that the utility of a major $NO^{\bullet}$ detoxification system in *Escherichia coli* (Hmp; $NO^{\bullet}$ dioxygenase) (Gardner et al., 1998; Stevanin et al., 2000), and thus the toxicity of $NO^{\bullet}$, depends highly on the $NO^{\bullet}$ delivery rate (Robinson and Brynildsen, 2013). This phenomenon suggests that $NO^{\bullet}$ payloads of the same total quantity but different delivery rates can vary remarkably in their cytotoxicity toward bacteria.

Here, we used quantitative kinetic modeling to explore the relationship between $NO^{\bullet}$ delivery rate, total payload, and antimicrobial activity as measured by the duration of respiratory inhibition by $NO^{\bullet}$. The model predicted that a faster release of $NO^{\bullet}$ is more effective at low payloads, whereas the opposite holds true at high payloads. These predictions were confirmed experimentally by measuring $NO^{\bullet}$ and O_2 consumption in batch cultures of *E. coli* following single or co-treatment with two $NO^{\bullet}$ donors with differing release kinetics. This work provides fundamental knowledge on the dependence of $NO^{\bullet}$ toxicity on delivery rate and total dose, which is a relationship that could prove useful for selection of $NO^{\bullet}$ dosing regimens for antimicrobial therapy.

2. Materials and methods

2.1. Kinetic modeling

Model simulations and analyses were performed in MATLAB (The MathWorks, Inc.). To simulate [$NO^{\bullet}$] and [O_2] dynamics, we employed a model of $NO^{\bullet}$ stress that we previously developed (Robinson and Brynildsen, 2013), and added a respiratory module that allowed simulation of O_2 consumption from the batch culture system.

* Correspondence to: 205 Hoyt Laboratory, 25 William Street, Princeton, NJ 08544, USA. Tel.: +1 609 258 1995; fax: +1 609 258 0211.
E-mail address: mbrynild@princeton.edu (M.P. Brynildsen).

http://dx.doi.org/10.1016/j.meteno.2014.08.001

2.1.1. Incorporation of a respiratory module

Aerobic respiration was incorporated through the addition of 4 reactions (NADH dehydrogenases NDH-1 and NDH-2, and O_2 consumption by cytochromes *bo* and *bd*-I), 14 kinetic parameters, and 4 species (Table S1). The third *E. coli* cytochrome oxidase, *bd*-II, was not included, as its activation is generally limited to conditions of phosphate starvation, entry into stationary phase, or anaerobiosis (Atlung and Brondsted, 1994; Dassa et al., 1991). NADH dehydrogenase I (NDH-I) contains 9 iron-sulfur ([Fe–S]) clusters (two [2Fe–2S] and seven [4Fe–4S]) (Euro et al., 2008), and therefore could potentially be inhibited by $NO^{\bullet}$, which is known to react rapidly with [Fe–S] clusters (Gardner et al., 1997; Foster and Cowan, 1999; Crack et al., 2011). This effect was addressed by incorporating a term into the NDH-1 rate equation which scales the reaction rate by the ratio of undamaged to total [Fe–S] clusters. Of the respiratory kinetic parameters, 4 were found to be variable within the literature, and only approximate concentrations of NADH dehydrogenases I and II, ubiquinone-8, ubiquinol-8 and cytochromes *bo* and *bd* were available. We therefore optimized this set of 10 uncertain parameters with experimentally-measured $[O_2]$ data from aerobic, exponential-phase *E. coli* cultivated in our system in the absence of nitrosative stress (Table S2 and Fig. S1).

2.1.2. Simulation of NONOate co-administration

To simulate the simultaneous delivery of two NONOates with different $NO^{\bullet}$-release kinetics, an additional NONOate species and dissociation reaction were incorporated into the model.

2.2. Experimental measurements

2.2.1. Chemicals

The growth media used in all experiments was MOPS minimal media (Teknova) with 10 mM glucose. DPTA NONOate, (Z)-1-[*N*-(3-aminopropyl)-*N*-(3-ammoniopropyl)amino]diazen-1-ium-1,2-diolate, and PAPA NONOate, (Z)-1-[*N*-(3-aminopropyl)-*N*-(n-propyl)amino]diazen-1-ium-1,2-diolate (Cayman Chemical), were dissolved in ice-cold 10 mM NaOH prior to use. Potassium cyanide (KCN; Sigma Life Science) was dissolved in sterile, deionized H_2O at a concentration of 1 M.

2.2.2. Bacterial strains

All experiments in this study were performed with *E. coli* K-12 MG1655.

2.2.3. Bioreactor

A disposable batch bioreactor, identical to that described previously (Robinson and Brynildsen, 2013), was used to facilitate measurements with the $NO^{\bullet}$ and O_2 sensors. Briefly, the bioreactor consisted of a sterile, 50 mL polypropylene conical tube (Falcon®) suspended in a magnetically-stirred water bath maintained at 37 °C. The 50 mL conical tube was open to the air, contained 10 mL of culture, and was stirred with a 0.5 in. magnetic stir bar.

2.2.4. Detection of $NO^{\bullet}$ and O_2

The concentrations of $NO^{\bullet}$ and O_2 were measured continuously ($\geq$1 sample per second) in the bioreactor culture using a $NO^{\bullet}$ sensor (2 mm ISO-NOP, World Precision Instruments, Inc.) and an O_2 sensor (3 mm OXROB10 Oxygen Probe with FireStingO2 meter, PyroScience GmbH), respectively. The sensors were suspended approximately 3 mm below the culture liquid surface, and clamped in place throughout the duration of the assay.

2.2.5. $NO^{\bullet}$ stress assay

Bacterial growth and $NO^{\bullet}$ treatment methods and conditions were identical to those reported previously (Robinson and Brynildsen, 2013), with two modifications to facilitate O_2 measurements: (1) cells were treated with $NO^{\bullet}$ immediately after resuspension in the bioreactor rather than allowing a ~45 min adjustment period before treatment, to ensure greater consistency among initial $[O_2]$; (2) the cells were delivered to a final OD_{600} of 0.1 rather than 0.05, to amplify $[O_2]$ changes caused by cellular processes, and thus improve their detection. For the KCN-treated O_2 consumption assay (Fig. S2), 1 mM KCN was delivered to the cells during resuspension, and to the 10 mL of fresh media in the bioreactor prior to inoculation.

2.2.6. Measurement of extracellular parameters

Kinetic parameters associated with extracellular processes specific to the experimental system were determined from $[O_2]$ and $[NO^{\bullet}]$ measurements in cell-free growth media (Table S3), as described previously (Robinson and Brynildsen, 2013). Briefly, the volumetric mass transfer coefficient of O_2 (k_La_{O2}) was calculated from the $[O_2]$ curve following media degassing with N_2. The $NO^{\bullet}$ volumetric mass transfer coefficient ($k_La_{NO\cdot}$), autoxidation rate constant ($k_{NO\cdot-O_2}$), and dissociation rate of DPTA ($k_{NONOate,DPTA}$), were optimized to fit the $[NO^{\bullet}]$ curve and final (12 h) NO_2^- concentration resulting from the addition of 500 μM DPTA to cell-free media (Fig. S3). The dissociation rate of PAPA ($k_{NONOate,PAPA}$) was also determined, using an $[NO^{\bullet}]$ curve measured following the treatment of cell-free media with 500 μM PAPA (Fig. S3).

2.3. Parametric analysis and optimization

2.3.1. Optimization of uncertain cellular parameters

Uncertain parameters were defined as those whose value varied widely in the literature, or were unavailable. Given the difference in $NO^{\bullet}$ treatment protocol from our previous study (Robinson and Brynildsen, 2013) (dosing immediately after resuspension into the bioreactor, rather than allowing a pre-growth period), as well as the inclusion of the new respiratory module and an additional dataset ($[O_2]$ curve), 37 uncertain cellular parameters were optimized to simultaneously capture the $[NO^{\bullet}]$ and $[O_2]$ dynamics of an aerobic, exponential-phase *E. coli* culture treated with 500 μM DPTA (Table S4). The optimization procedure was identical to the previous approach except that $[O_2]$ data was included and optimized simultaneously with the $[NO^{\bullet}]$ curve. The set of parameter values yielding the minimum sum of the squared residuals (SSR) between experimental and simulated $[NO^{\bullet}]$ and $[O_2]$ curves were selected as the optimal set.

2.3.2. Parametric analysis

Parametric analyses were conducted to determine which parameters were informed from the optimization of the respiratory module with untreated O_2 consumption data (Table S2), and optimization of the cellular parameters with the 500 μM DPTA $[NO^{\bullet}]$ and $[O_2]$ curves (Table S4). Parameters were individually varied within their literature or physiological ranges, and the resulting effect on SSR between simulated and measured concentrations was calculated. Those exhibiting at least a 5% change in SSR were considered to be informed as a result of the optimization.

3. Results

Given the importance of $NO^{\bullet}$ delivery kinetics on the distribution of $NO^{\bullet}$ in *E. coli* (Robinson and Brynildsen, 2013), we used a quantitative kinetic model to explore the relationship between $NO^{\bullet}$ delivery rate and antimicrobial efficacy, and examined how this relationship is affected by total $NO^{\bullet}$ payload. One of the key

antimicrobial properties of NO• is its potent inhibition of respiration through reversible binding with the cytochrome terminal oxidases. The importance of this effect is emphasized by the *E. coli* transcriptional response to NO•, where cytochrome *bd*, which has been found to confer resistance to NO• due to its higher NO• off-rate (Mason et al., 2009), is strongly upregulated following NO• treatment (Hyduke et al., 2007; Pullan et al., 2007). Therefore, duration of respiratory inhibition was used here as a metric of the antimicrobial activity of NO•. In order to quantify the activity of cellular respiration, the model required augmentation with a respiratory module to simulate respiration-mediated O_2 consumption.

3.1. Simulation of aerobic respiration

Respiration was incorporated into an existing kinetic model of NO• stress in *E. coli* (Robinson and Brynildsen, 2013) through the addition of NADH dehydrogenases and cytochrome-mediated reduction of O_2 (Table S1). Although the previous model included reversible binding of cytochromes *bo* and *bd* with NO•, it did not include rate expressions necessary to quantify the impact of respiration on O_2 consumption. O_2 reduction (coupled with ubiquinol oxidation) was added for both cytochromes, and the NADH dehydrogenases (NDH-1 and NDH-2) were incorporated to reduce the quinone pool through NADH oxidation (see Section 2.1.1). A set of 10 uncertain respiratory kinetic parameters and species concentrations were optimized to reproduce the $[O_2]$ curve measured in a culture of aerobic, exponential-phase *E. coli* in our experimental system (Fig. S1). A parametric analysis of the optimized respiratory parameters revealed that all 10 parameters substantially influenced the error between the measured and simulated $[O_2]$ curve ($>5\%$ increase in SSR), and thus were considered informed by the optimization process. In addition, O_2 consumption was also measured in a culture treated with 1 mM KCN to inhibit respiration. In the presence of KCN, negligible O_2 consumption was observed, confirming that respiration was responsible for the measured consumption of O_2 (Fig. S2).

3.2. Respiration of NO•-treated E. coli

After implementing the respiratory component into the model, we sought to explore the relationship between NO• delivery rate, total NO• delivered, and antimicrobial activity. In order to investigate this relationship, it was necessary to train the model on experimental data obtained from a single condition and use it to extrapolate to other dosing scenarios. Uncertain cellular parameters (37) were trained on [NO•] and $[O_2]$ curves measured in a culture of aerobic, exponential-phase *E. coli* treated with 500 μM DPTA (Table S4), and the resulting optimized model simulations exhibited excellent agreement with measurements (Fig. 1A and B). A parametric analysis was conducted to investigate which parameters were informed by the optimization, and revealed that 14 of the optimized parameters significantly influenced the SSR between the measured and simulated [NO•] and $[O_2]$ curves. These parameters were involved in Hmp activity ($k_{\mathrm{Hmp,NO\cdot\_on}}$) and expression ($k_{\mathrm{Hmp\text{-}exp,max}}$, $K_{\mathrm{Hmp-exp,NO\cdot}}$), O_2-mediated inactivation of NorV ($k_{\mathrm{NorV-O_2}}$), as well as [Fe–S] cluster concentration ($[P_{\mathrm{2Fe2S}}(holo)]_0$, $[P_{\mathrm{4Fe4S}}(holo)]_0$), damage ($k_{\mathrm{NO\cdot\_[Fe-S]}}$), and repair ($k_{\mathrm{DNIC\text{-}rem}}$, $k_{\mathrm{IscU\text{-}load\text{-}Fe}}$, $K_{\mathrm{IscU\text{-}load\text{-}S,IscU}}$, $k_{\mathrm{IscU\text{-}2Fe2S\text{-}insert,cat}}$, $k_{\mathrm{IscU\text{-}4Fe4S\text{-}insert}}$, $[\mathrm{IscU}]_0$, $[\mathrm{IscS}]_0$). It is important to note that [Fe–S]

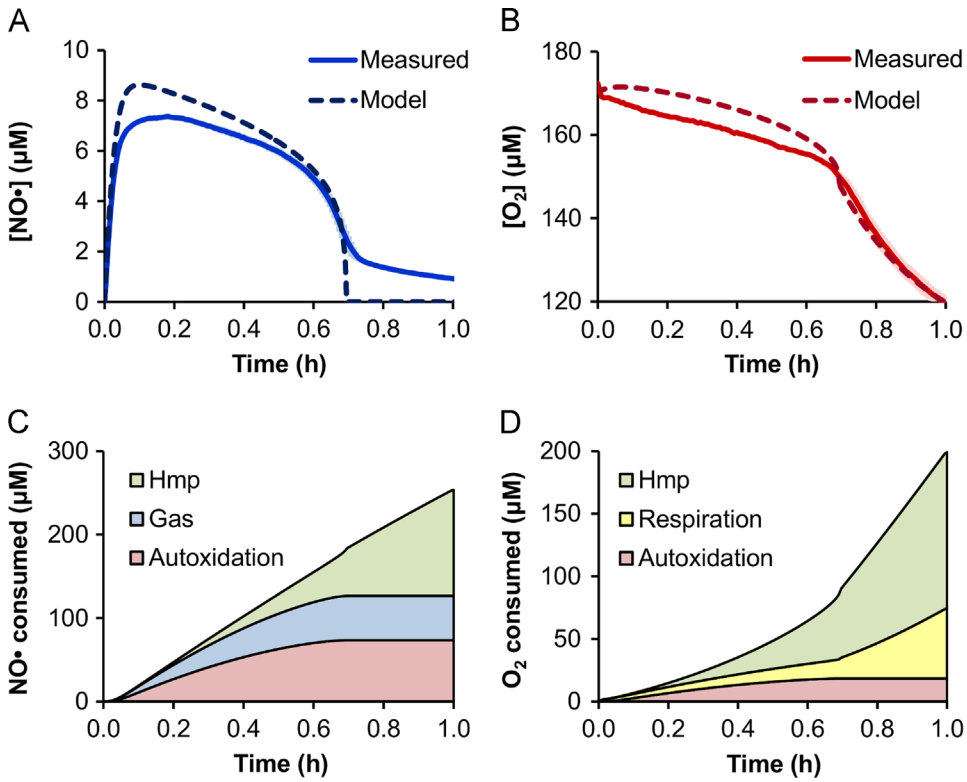

Fig. 1. Measured and optimized [NO•] and $[O_2]$ dynamics. Shown are the (A) [NO•] curves and (B) $[O_2]$ curves measured experimentally (solid lines) and simulated by the optimized model (dashed lines) for an aerobic culture of *E. coli* treated with 500 μM DPTA at time zero. Measured concentration curves are the mean of 3 independent experiments, where light blue (NO•) or light red (O_2) error bars represent the standard error of the mean. The corresponding predicted distributions of cumulative (C) NO• and (D) O_2 consumption are shown for the major consumption pathways, which account for over 99% of the total NO• or O_2 consumption in the first hour after treatment. "Hmp" indicates consumption by Hmp-mediated NO• detoxification, "Gas" is NO• lost to the gas phase, "Autoxidation" is autoxidation of NO• with O_2 in the media, and "Respiration" is total O_2 consumed by cytochrome oxidase (*bo* and *bd*) activity. (For interpretation of the references to color in this figure legend, the reader is referred to the web version of this article.)

nitrosylation and repair kinetics are specific to the surrounding protein environment (Varghese et al., 2003; Crack et al., 2012), and the parameter values obtained here were informed specifically for NDH-1 activity, and therefore do not necessarily reflect the dynamics of [Fe–S] clusters contained in other proteins. Of the 14 parameters, only the first 4 (Hmp- and NorV-related parameters) had a significant impact on both the simulated [NO•] and [O_2] curves, while the remaining 10 [Fe–S] cluster-related parameters influenced only the [O_2] curve.

In order to better understand the pathways contributing to the simulated dynamics, the associated distributions of NO• and O_2 consumption were calculated. The predicted contributions by the major pathways are shown in Fig. 1C and D. The NO• consumption is initially predicted to be dominated by autoxidation in the media and loss to the gas phase, while Hmp accounts for the majority of NO• clearance at later times. Because Hmp uses O_2 to detoxify NO• to NO_3^- (Gardner et al., 2000), it is also predicted to account for a substantial portion of the cellular O_2 consumption (Fig. 1D). However, after the [NO•] drops and cytochrome inhibition is relieved, the contribution of respiration to O_2 consumption begins to approach that of Hmp, and overtakes it by 1.5 h. The impact of the respiratory component on the predicted [O_2] curve is further illustrated in Fig. S4, which shows poor agreement with the experimental [O_2] data when the respiratory component is excluded.

3.3. Evaluation of delivery regimens

3.3.1. Simulated delivery regimens

Once accurate model performance had been confirmed, we sought to examine the dynamics of various delivery regimens. We used the model to simulate delivery of NO• to a culture of *E. coli* *via* co-administration of two NONOates with different NO• release rates, DPTA (slower release, $k_{NONOate,DPTA}=8.24\times10^{-5}\ s^{-1}$) and PAPA (faster release, $k_{NONOate,PAPA}=7.35\times10^{-4}\ s^{-1}$) (see Section 2.2.6 for details regarding NONOate release rate measurements). The fraction of delivered NONOate comprised of DPTA (x_{DPTA}) was varied from 0 to 1 (with a balance of PAPA), while total NONOate concentrations were varied from 100 μM to 1500 μM. The scan was conducted by varying only initial DPTA and PAPA concentrations for each condition – all other parameters were fixed. Relief of NO•-mediated respiration inhibition was used as the biological indicator of bacterial recovery from NO• stress, and was defined as the time (t_{rec}) at which the concentration of NO•-bound cytochromes (*bo* and *bd*) dropped below 50% of the total cytochrome concentration, which also coincided with an abrupt slope change in both the [O_2] and [NO•] curves (Fig. 2A and B).

The simulations revealed a monotonic change in t_{rec} with respect to [NONOate], and to x_{DPTA} (Fig. 2C). Interestingly, it was predicted that administration of only DPTA ($x_{DPTA}=1$) would yield the optimal inhibitory effect at higher payloads (2.23 h for 1500 μM DPTA compared to 1.24 h for 1500 μM PAPA), while the opposite held true at low payloads (0.15 h for 100 μM DPTA compared to 0.46 h for 100 μM PAPA).

3.3.2. Experimental validation of simulated delivery regimens

To validate the model predictions experimentally, cultures of *E. coli* were treated with 3 different total NONOate concentrations ([NONOate]=100, 500, and 1500 μM) and 3 different fractions of DPTA ($x_{DPTA}=0$, 0.5, and 1), for a total of 9 combinations that spanned the bounds of the simulations. [NO•] and [O_2] were measured continuously, and compared with the predicted concentration profiles. Overall, the model simulations accurately captured both the [NO•] and [O_2] dynamics for all 9 conditions (Fig. 3). Predictions at 500 and 100 μM [NONOate] were in excellent agreement with measurements for both [NO•] and [O_2] curves, though the model overestimated the [NO•] peak value for the 100 μM DPTA condition. A potential cause could be a low but nonzero initial concentration of Hmp (assumed to be zero in the model (Stevanin et al., 2000; Poole et al., 1996)) present in the cells prior to NO• treatment, which would be able to quickly eliminate low concentrations of slowly-released NO•, but impart a negligible effect on the [NO•] curves at higher NONOate concentrations and release rates. The measured [NO•] and [O_2] dynamics were also in good agreement with predictions at higher [NONOate] (1500 μM), though the quantitative differences were more pronounced in some cases relative to those of lower [NONOate].

To identify t_{rec} from experimental data, the [O_2] and [NO•] curves were inspected for a simultaneous abrupt slope change, analogous to that observed in the simulated concentration curves at the point of respiratory relief (Fig. 2A and B). Given the reactivity of NO• with [Fe–S] clusters, enzymes beyond NDH-1 and the cytochrome terminal oxidases were likely inhibited by NO•. To exclude the possibility that such enzymes could consume O_2 at a rate fast enough to drop the culture-wide [O_2], we measured [O_2] in respiratory-inhibited (KCN-treated) cultures. As

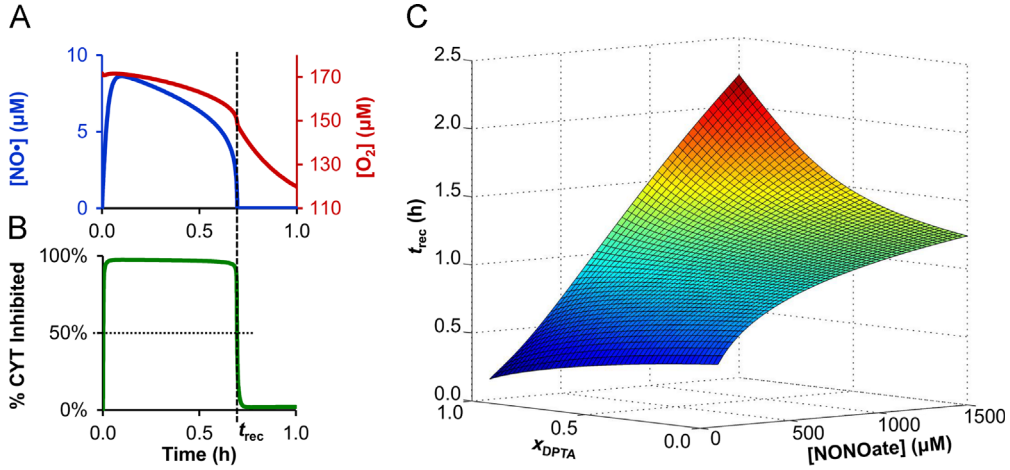

Fig. 2. Simulations of NO• dosing regimens. Predicted (A) [NO•] and [O_2] curves, and (B) fraction of total cytochromes (CYT) inhibited (bound with NO•) are shown for the treatment of *E. coli* with 500 μM DPTA. The dotted horizontal line in (B) indicates 50% cytochrome inhibition by NO•, with the vertical dashed line indicating the time at which inhibition drops below 50%, which is defined as the time of respiration recovery (t_{rec}). The vertical dashed line extends into (A) to highlight the simultaneous abrupt slope change in the predicted [O_2] and [NO•] curves that coincides with t_{rec}. (C) A surface plot shows the predicted t_{rec} values as a function of total NO• payload ([NONOate]) and fraction of [NONOate] comprised of DPTA (x_{DPTA}) for simulations ranging from 100 μM to 1500 μM [NONOate], and 0 to 1 x_{DPTA}.

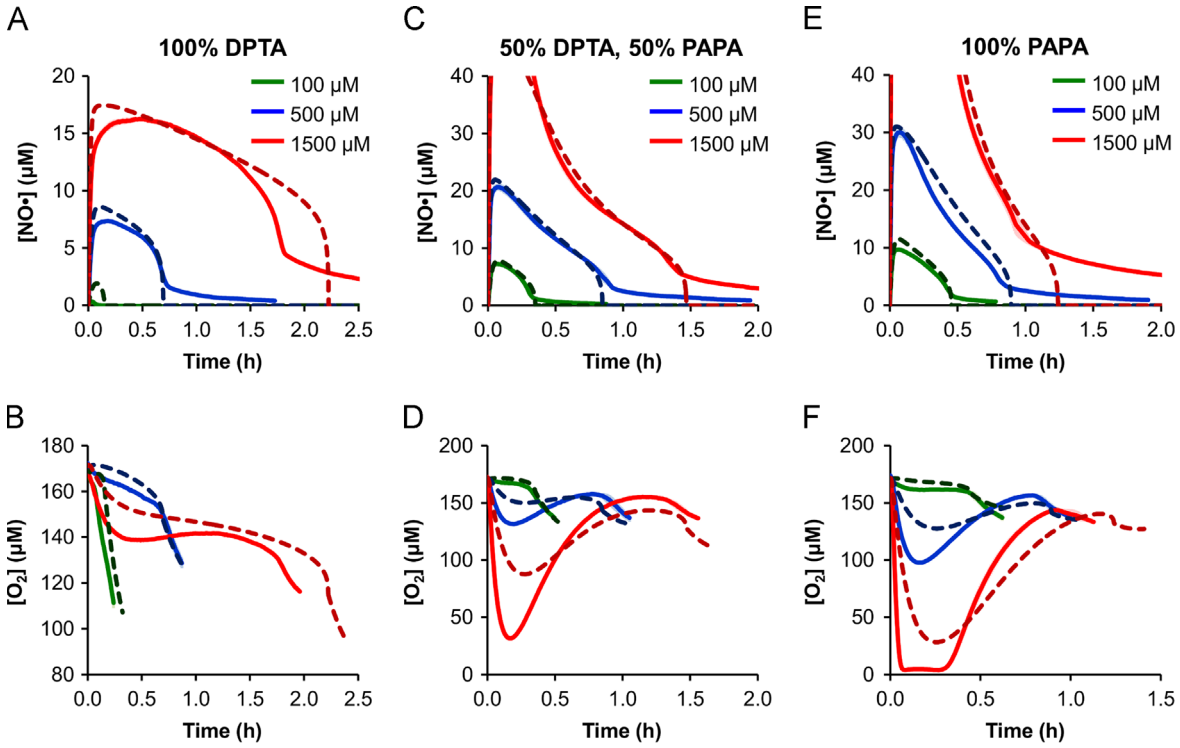

Fig. 3. [NO•] and [O_2] dynamics at various dosing regimens. Simulated (dashed lines) and measured (solid lines) [NO•] curves (top row) and [O_2] curves (bottom row) are shown following treatment of *E. coli* cultures with 100% DPTA (A and B), 50% DPTA+50% PAPA (C and D), or 100% PAPA (E and F) at total NONOate concentrations of 100 μM (green lines), 500 μM (blue lines), or 1500 μM (red lines). Measured concentrations are the mean of 3 independent experiments, with light green, light blue, or light red error bars representing the standard error of the mean. [NO•] is not reported above 40 μM, because per the manufacturer's specifications, the probe does not accurately quantify [NO•] > 40 μM. Nonzero "tails" at the end of [NO•] curves are an artifact of delayed electrode responses associated with returning the signal to baseline after prolonged exposure to high [NO•]. The [O_2] curves are shown up to 10 min following respiration recovery (t_{rec}), as growth resumes and is not accounted for in the model. (For interpretation of the references to color in this figure legend, the reader is referred to the web version of this article.)

depicted in Fig. S2, respiratory-inhibited cultures exhibited negligible O_2 consumption, demonstrating that enzymatic activities beyond respiration do not consume O_2 at a sufficient rate to produce an abrupt decline in culture-wide [O_2]. This data confirms that relief of respiration was responsible for the observed increase in O_2 consumption that coincided with NO• clearance. We note that [O_2] measurements from KCN-treated cultures were performed in the absence of NO•, because KCN also inhibits Hmp (Stevanin et al., 2000), thereby precluding its use for specific elimination of respiratory contributions to O_2 consumption in the presence of NO•.

The experimentally-measured recovery times (t_{rec}) confirmed the model prediction that DPTA (slower NO• release rate) would exhibit greater cytotoxicity at higher NONOate concentrations, while PAPA (faster NO• release rate) would exhibit a stronger effect at lower concentrations, with little difference between the two at 500 μM (Fig. 4). Not only did the model successfully capture the trends for each condition, but the predicted t_{rec} values exhibited excellent quantitative agreement with the experimental measurements.

4. Discussion

Using a quantitative kinetic model, we investigated the relationship between NO• delivery rate to an *E. coli* culture, total NO• payload, and antimicrobial activity (defined as duration of respiratory inhibition). The model predicted that the antimicrobial activity of different payloads was dependent on the dosing kinetics, and we confirmed this phenomenon experimentally. These results may have important ramifications for materials designed to deliver NO• to infection sites. NO•-releasing nanoparticles, which have already been shown to exhibit antimicrobial activity against a diversity of clinically-relevant pathogens (*e.g.*, methicillin-resistant *Staphylococcus aureus* (MRSA) (Han et al., 2009), multidrug-resistant *Acinetobacter baumannii* (Mihu et al., 2010), *Pseudomonas aeruginosa*, *E. coli*, and *Streptococcus pyogenes* (A. Friedman et al., 2011)), provide a tunable delivery vehicle that allows modulation of total NO• payload and NO• release rate (Friedman et al., 2008). Similarly, enzymatic NO•-releasing dressings, which have been proven effective in treating MRSA, *P. aeruginosa*, and *A. baumannii* biofilms (Sulemankhil et al., 2012), can be formulated with variable NO• payloads and release rates. These and other NO•-releasing materials, which have shown potential in animal studies (Han et al., 2009; Martinez et al., 2009; Nablo et al., 2005) and pilot studies with human subjects (Ormerod et al., 2011; Phillips et al., 2004), would benefit from a quantitative understanding of how two relevant and readily-tunable design parameters influence treatment efficacy.

In addition to delivery kinetics and payload, numerous other parameters, such as donor type (*e.g.*, S-nitrosothiols, acidified nitrite), O_2 tension, pH, bacterial species, hydrophobicity, and presence of other radicals, influence the kinetic competition for NO• in biological systems (Bowman et al., 2011; Robinson et al., 2014; Toledo Jr. and Augusto, 2012; Jarboe et al., 2008). NO• is also a potent signaling molecule in mammalian systems that could alter the host environment surrounding pathogens, and thereby impact NO• detoxification (Toledo Jr. and Augusto 2012; Nathan, 1992). Given this complexity, quantitative models are useful to understand and predict how environmental and cellular parameters influence cytotoxicity (Robinson et al., 2014). The structure and content of the model used here are readily modified (*e.g.*, parameter adjustment, reaction addition/removal, or change in compartmentalization) to represent a target condition, such as an

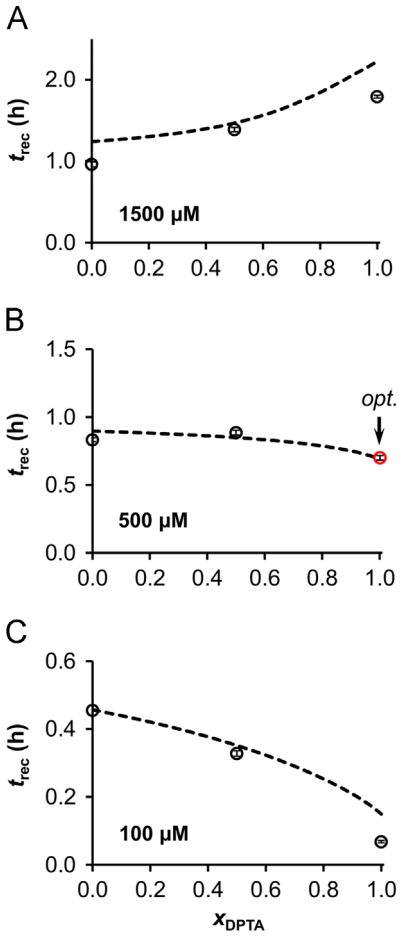

Fig. 4. The influence of dose regimen on NO• toxicity is accurately predicted. Shown are the predicted (dashed lines) and experimentally-measured (open circles) t_{rec} values as a function of x_{DPTA} for total NONOate concentrations of (A) 1500 μM, (B) 500 μM, and (C) 100 μM. The measured t_{rec} values are the mean of 3 independent experiments, with error bars representing the standard error of the mean. A red circle indicates the condition on which the model was trained. (For interpretation of the references to color in this figure legend, the reader is referred to the web version of this article.)

O_2-rich dermal surface or a particular pathogenic subspecies. The quantitative knowledge of NO• cytotoxicity offered by these models could prove useful in enhancing the potency of NO•-based therapeutics for the treatment of bacterial infections.

Acknowledgments

This work was supported in part by the National Science Foundation Graduate Research Fellowship Program under Grant no. DGE 1148900, and with funds from the Princeton University (Forese Family Fund for Innovation and start-up funds).

Appendix A. Supplementary information

Supplementary data associated with this article can be found in the online version at http://dx.doi.org/10.1016/j.meteno.2014.08.001.

References

Atlung, T., Brondsted, L., 1994. Role of the transcriptional activator AppY in regulation of the Cyx AppA operon of *Escherichia coli* by anaerobiosis, phosphate starvation, and growth-phase. J. Bacteriol. 176, 5414–5422.

Bogdan, C., 2001. Nitric oxide and the immune response. Nat. Immunol. 2, 907–916.

Bowman, L.A.H., McLean, S., Poole, R.K., Fukuto, J.M., 2011. The diversity of microbial responses to nitric oxide and agents of nitrosative stress: close cousins but not identical twins. Adv. Microb. Physiol. 59, 135–219.

Crack, J.C., Smith, L.J., Stapleton, M.R., Peck, J., Watmough, N.J., Buttner, M.J., Buxton, R.S., Green, J., Oganesyan, V.S., Thomson, A.J., et al., 2011. Mechanistic insight into the nitrosylation of the [4Fe–4S] cluster of WhiB-like proteins. J. Am. Chem. Soc. 133, 1112–1121.

Crack, J.C., Green, J., Thomson, A.J., Le Brun, N.E., 2012. Iron–sulfur cluster sensor-regulators. Curr. Opin. Chem. Biol. 16, 35–44.

Dassa, J., Fsihi, H., Marck, C., Dion, M., Kieffer-Bontemps, M., Boquet, P.L., 1991. A new oxygen-regulated operon in *Escherichia coli* comprises the genes for a putative third cytochrome oxidase and for pH 2.5 acid phosphatase (appA). Mol. Gen. Genet. 229, 341–352.

Euro, L., Bloch, D.A., Wikstrom, M., Verkhovsky, M.I., Verkbovskaya, M., 2008. Electrostatic interactions between FeS clusters in NADH: ubiquinone oxidoreductase (complex I) from *Escherichia coli*. Biochemistry 47, 3185–3193.

Fang, F.C., 2004. Antimicrobial reactive oxygen and nitrogen species: concepts and controversies. Nat. Rev. Microbiol. 2, 820–832.

Foster, H.W., Cowan, J.A., 1999. Chemistry of nitric oxide with protein-bound iron sulfur centers. Insights on physiological reactivity. J. Am. Chem. Soc. 121, 4093–4100.

Friedman, A., Blecher, K., Sanchez, D., Tuckman-Vernon, C., Gialanella, P., Friedman, J.M., Martinez, L.R., Nosanchuk, J.D., 2011. Susceptibility of Gram-positive and -negative bacteria to novel nitric oxide-releasing nanoparticle technology. Virulence 2, 217–221.

Friedman, A.J., Han, G., Navati, M.S., Chacko, M., Gunther, L., Alfieri, A., Friedman, J. M., 2008. Sustained release nitric oxide releasing nanoparticles: characterization of a novel delivery platform based on nitrite containing hydrogel/glass composites. Nitric Oxide 19, 12–20.

Friedman, A.J., Blecher, K., Schairer, D., Tuckman-Vernon, C., Nacharaju, P., Sanchez, D., Gialanella, P., Martinez, L.R., Friedman, J.M., Nosanchuk, J.D., 2011. Improved antimicrobial efficacy with nitric oxide releasing nanoparticle generated S-nitrosoglutathione. Nitric Oxide 25, 381–386.

Gardner, A.M., Martin, L.A., Gardner, P.R., Dou, Y., Olson, J.S., 2000. Steady-state and transient kinetics of *Escherichia coli* nitric-oxide dioxygenase (flavohemoglobin) – the B10 tyrosine hydroxyl is essential for dioxygen binding and catalysis. J. Biol. Chem. 275, 12581–12589.

Gardner, P.R., Costantino, G., Szabo, C., Salzman, A.L., 1997. Nitric oxide sensitivity of the aconitases. J. Biol. Chem. 272, 25071–25076.

Gardner, P.R., Gardner, A.M., Martin, L.A., Salzman, A.L., 1998. Nitric oxide dioxygenase: an enzymic function for flavohemoglobin. Proc. Natl. Acad. Sci. USA 95, 10378–10383.

Han, G., Martinez, L.R., Mihu, M.R., Friedman, A.J., Friedman, J.M., Nosanchuk, J.D., 2009. Nitric oxide releasing nanoparticles are therapeutic for *Staphylococcus aureus* Abscesses in a murine model of infection. PLoS One 4, e7804.

Hyduke, D.R., Jarboe, L.R., Tran, L.M., Chou, K.J.Y., Liao, J.C., 2007. Integrated network analysis identifies nitric oxide response networks and dihydroxyacid dehydratase as a crucial target in *Escherichia coli*. Proc. Natl. Acad. Sci. USA 104, 8484–8489.

Jarboe, L.R., Hyduke, D.R., Tran, L.M., Chou, K.J.Y., Liao, J.C., 2008. Determination of the *Escherichia coli* S-nitrosoglutathione response network using integrated biochemical and systems analysis. J. Biol. Chem. 283, 5148–5157.

Jones, M.L., Ganopolsky, J.G., Labbe, A., Wahl, C., Prakash, S., 2010. Antimicrobial properties of nitric oxide and its application in antimicrobial formulations and medical devices. Appl. Microbiol. Biotechnol. 88, 401–407.

Martinez, L.R., Han, G., Chacko, M., Mihu, M.R., Jacobson, M., Gialanella, P., Friedman, A.J., Nosanchuk, J.D., Friedman, J.M., 2009. Antimicrobial and healing efficacy of sustained release nitric oxide nanoparticles against *Staphylococcus aureus* skin infection. J. Investig. Dermatol. 129, 2463–2469.

Mason, M.G., Shepherd, M., Nicholls, P., Dobbin, P.S., Dodsworth, K.S., Poole, R.K., Cooper, C.E., 2009. Cytochrome bd confers nitric oxide resistance to *Escherichia coli*. Nat. Chem. Biol. 5, 94–96.

Mihu, M.R., Sandkovsky, U., Han, G., Friedman, J.M., Nosanchuk, J.D., Martinez, L.R., 2010. Nitric oxide releasing nanoparticles are therapeutic for *Acinetobacter baumannii* wound infections. Virulence 1, 62–67.

Nablo, B.J., Prichard, H.L., Butler, R.D., Klitzman, B., Schoenfisch, M.H., 2005. Inhibition of implant-associated infections via nitric oxide release. Biomaterials 26, 6984–6990.

Nathan, C., 1992. Nitric oxide as a secretory product of mammalian cells. FASEB J. 6, 3051–3064.

Ormerod, A.D., Shah, A.A., Li, H., Benjamin, N.B., Ferguson, G.P., Leifert, C., 2011. An observational prospective study of topical acidified nitrite for killing methicillin-resistant *Staphylococcus aureus* (MRSA) in contaminated wounds. BMC Res. Notes 4, 458.

Phillips, R., Adjei, O., Lucas, S., Benjamin, N., Wansbrough-Jones, M., 2004. Pilot randomized double-blind trial of treatment of *Mycobacterium ulcerans* disease (Buruli ulcer) with topical nitrogen oxides. Antimicrob. Agents Chemother. 48, 2866–2870.

Poole, R.K., Anjum, M.F., MembrilloHernandez, J., Kim, S.O., Hughes, M.N., Stewart, V., 1996. Nitric oxide, nitrite, and Fnr regulation of hmp (Flavohemoglobin) gene expression in *Escherichia coli* K-12. J. Bacteriol. 178, 5487–5492.

Pullan, S.T., Gidley, M.D., Jones, R.A., Barrett, J., Stevanin, T.A., Read, R.C., Green, J., Poole, R.K., 2007. Nitric oxide in chemostat-cultured *Escherichia coli* is sensed by Fnr and other global regulators: unaltered methionine biosynthesis indicates lack of S nitrosation. J. Bacteriol. 189, 1845–1855.

Robinson, J.L., Brynildsen, M.P., 2013. A kinetic platform to determine the fate of nitric oxide in *Escherichia coli*. PLoS. Comput. Biol. 9, e1003049.
Robinson, J.L., Adolfsen, K.J., Brynildsen, M.P., 2014. Deciphering nitric oxide stress in bacteria with quantitative modeling. Curr. Opin. Microbiol. 19C, 16–24.
Schairer, D.O., Chouake, J.S., Nosanchuk, J.D., Friedman, A.J., 2012. The potential of nitric oxide releasing therapies as antimicrobial agents. Virulence 3, 271–279.
Stevanin, T.M., Ioannidis, N., Mills, C.E., Kim, S.O., Hughes, M.N., Poole, R.K., 2000. Flavohemoglobin Hmp affords inducible protection for *Escherichia coli* respiration, catalyzed by cytochromes bo′ or bd, from nitric oxide. J. Biol. Chem. 275, 35868–35875.
Sulemankhil, I., Ganopolsky, J.G., Dieni, C.A., Dan, A.F., Jones, M.L., Prakash, S., 2012. Prevention and treatment of virulent bacterial biofilms with an enzymatic nitric oxide-releasing dressing. Antimicrob. Agents Chemother. 56, 6095–6103.
Sun, B, Slomberg, DL, Chudasama, SL, Lu, Y, Schoenfisch, MH, 2012. Nitric oxide-releasing dendrimers as antibacterial agents. Biomacromolecules 13, 3343–3354.
Toledo Jr., J.C., Augusto, O., 2012. Connecting the chemical and biological properties of nitric oxide. Chem. Res. Toxicol. 25, 975–989.
Varghese, S., Tang, Y., Imlay, J.A., 2003. Contrasting sensitivities of *Escherichia coli* aconitases A and B to oxidation and iron depletion. J. Bacteriol. 185, 221–230.